International Atomic Energy Agency INDC(GER)-31/GX

INDC INTERNATIONAL NUCLEAR DATA COMMITTEE

ANGLE AND ENERGY DIFFERENTIAL CROSS SECTIONS FOR THE (p,xn) REACTIONS OF 25.6 MeV PROTONS WITH ^{92,94,95,96,97,98,100}Mo

E. Mordhorst, M. Trabandt, F. Binasch, A. Kaminsky, H. Krause
R. Langkau, W. Scobel and M. Strecker

I. Institut für Experimentalphysik, Zyklotron, Universität Hamburg,
D-2000 Hamburg 50, Fed. Rep. of Germany

May 1988

INDC(GER)-31/GX

ANGLE AND ENERGY DIFFERENTIAL CROSS SECTIONS FOR THE (p,xn) REACTIONS OF 25.6 MeV PROTONS WITH ^{92,94,95,96,97,98,100}Mo

E. Mordhorst, M. Trabandt, F. Binasch, A. Kaminsky, H. Krause
R. Langkau, W. Scobel and M. Strecker

I. Institut für Experimentalphysik, Zyklotron, Universität Hamburg,
D-2000 Hamburg 50, Fed. Rep. of Germany

May 1988

Abstract

Cross sections for the inclusive production of neutrons from reactions of 25.6 MeV protons with all stable molybdenum isotopes have been measured with time-of-flight techniques for 24 angles ranging from 3^{o} to 177^{o}. After a short presentation of the motivations for these measurements, the experimental set up is discussed with emphasis on the systematic and/or statistical uncertainties pertinent to this work.

Reproduced by the IAEA in Austria
May 1988

88-02165

I. Introduction

The data presented in this report have been taken to study nuclear structure effects in the inclusive preequilibrium (PE) neutron emission from proton induced reactions. The (p,n) residual nuclei range from $^{92}_{43}$Tc near the N=50 shell closure to $^{100}_{43}$Tc in the new region of deformation [2] at A ≈ 100 and include odd-odd as well as odd-even nuclei.

The interpretation [1] of these data focuses on three topics:

(i) The influence of the realistic partial state densities: Most semiclassical PE models are based on the assumption of an energy dissipation in nucleon-nucleon collisions in a nuclear Fermi-gas with equidistant single particle states. The entrance state is assumed to be composed of 2 particles and 1 hole. Most of the PE yield comes from this stage. Therefore the neutron energy spectra should be in first order proportional to the partial 1 proton-particle 1 neutron-hole state density $\rho_{1,1}(U)$ of the residual nuclei. In the equidistant Fermi gas model, $\rho_{1,1}(U)$ is a linear function of U, whereas realistic single particle level schemes lead to structured state densities $\rho_{1,1}$, in particular for nuclei with (almost) closed shells [3].

(ii) The influence of pairing and nuclear deformation: The results of Grimes et al. [4] show that for residual systems being $\Delta Z = 3$ away from the closed shell Z=50, the effect (i) is already significantly reduced, because the shell gap decreases rapidly with increasing deformation and the partial state densities change more when <u>one single</u> nucleon is added than with a <u>pair</u> of like nucleons. The pairing energies Δ that can account for this effect are larger than those in use for compound nucleus reactions;

they can be correlated with a nuclear deformation parameter δ necessary to generate Δ from a set of realistic Nilsson model single particle states for the partial state density $\rho_{l,\pi}(U)$.

(iii) The shapes of the angular distributions: The backward yield of neutrons from (p,xn) reactions cannot be understood in terms of semiclassical PE models [5], whereas quantum-mechanical models succeed in describing the angular distributions [6]. So far this question has not yet been studied for a sequence of target nucleons that would allow to separate structural effects of individual target isotopes from gross features due to nuclear matter and scaling due to increasing neutron excess N-Z.

In order to study these effects it is necessary to measure neutron energy spectra over a broad range of angles. The low yield of high energy neutrons under backward angles requires a careful treatment of the background. We want to keep the option to study the equilibrium component lateron by supplementing the present data with data taken at lower projectile energies; therefore we have performed the experiment with fairly low neutron energy thresholds.

The experimental set up is presented in Sect. 2.1. Measurements, sample data, data reduction and uncertainties are discussed in Sect. 2.2 and 2.3.

2. Apparatus and Measurements

2.1. Experimental set up

The experiment has been performed with the 25.6±0.15 MeV proton beam of the Hamburg Isochronous Cyclotron. The energy spread includes the effect of target thickness. The 19.27 MHz

repetition rate (cyclotron RF) was scaled down with an external deflection system [7] by a factor of 14 to allow for neutron time-of-flight (TOF) spectroscopy with flight paths of at most 8 m and neutron energies between 1 MeV and 25 MeV without ambiguities due to overlapping bursts.

The geometry of the neutron TOF area is shown in Fig. 1. The set up consists of 8 detectors and is designed for low background and large angular range performance [8]. For this purpose the proton beam is bent with two dipole magnets by 2×17^{o} out of the 0^{o} direction and then dumped into a heavily shielded (water, paraffine, lead) Faraday Cup. The yokes of the magnets are of C type with a gap width of 10 cm. The reaction chamber inserted into this gap has a shape corresponding to a 34^{o} segment of a circle. It has three remotely controlled target positions in front of, between and behind the two magnets. The integrated Faraday Cup current was recorded for absolute cross section determination.

Reaction neutrons from the target position in operation enter flight paths of (7.5±0.5) m length through a thin exit window (0.13 mm Kapton foil) towards the neutron detectors. The detectors consist of cylindrical 4"ø×2" cells filled with liquid scintillator NE213 and coupled to photomultipliers VALVO XP2041. They are viewing the targets through collimator tubes traversing a water shielding of more than 1 m thickness. Conical polyethylene throats at the front ends of the collimator tubes supplement the efficient shielding against time correlated and stray neutrons. The collimator tubes can be aligned towards any of the three optional target positions such that the set up covers an interval of reaction angles Θ ranging from 3^{o} to 177^{o} with

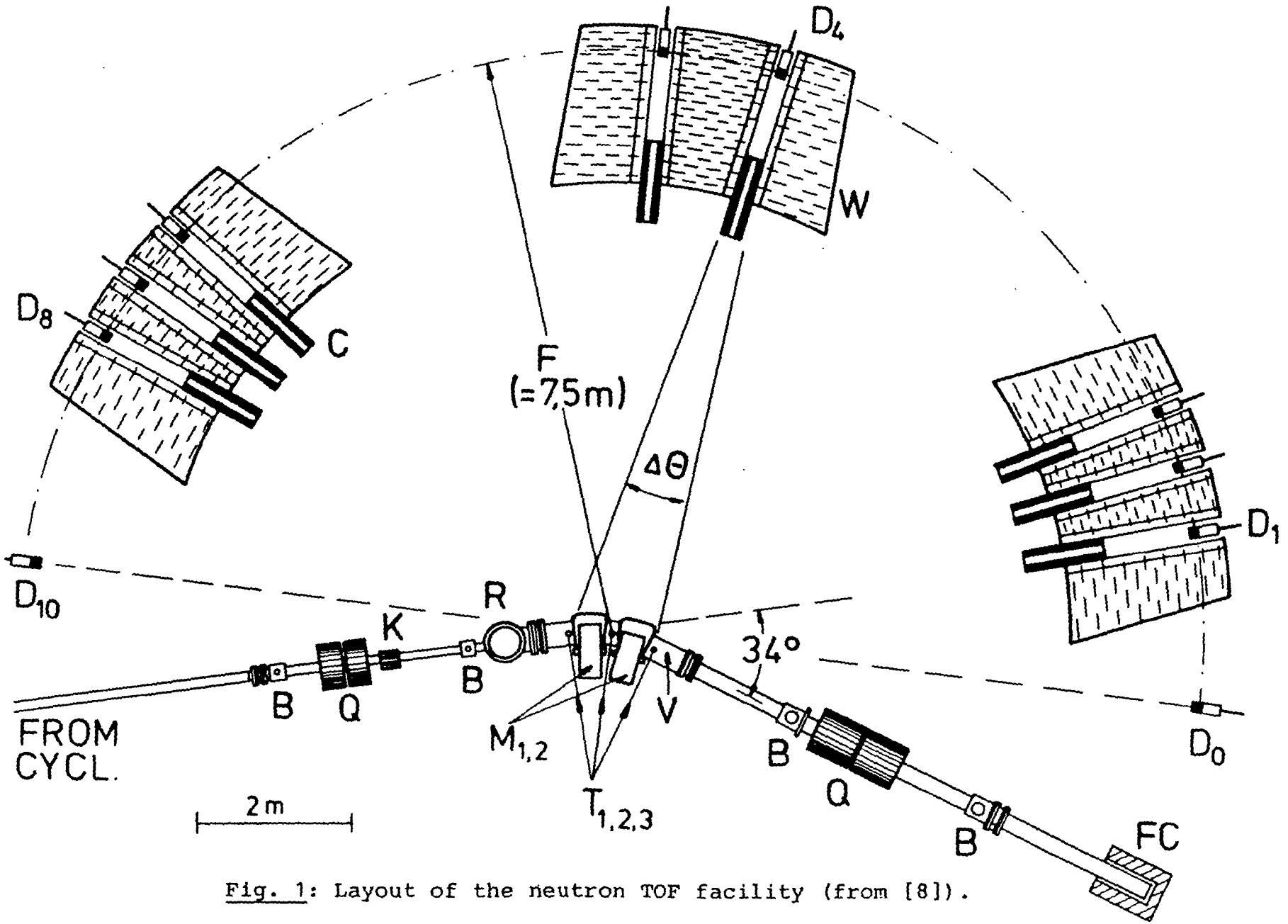

Fig. 1: Layout of the neutron TOF facility (from [8]).

24 fixed positions and increments of 6.5° for small and large, and 10.5° for intermediate angles, respectively.

The targets were self-supporting, isotopically enriched metallic foils of 12 mm effective diameter and nominal thicknesses ranging from 3.0 to 4.9 mg/cm^2 (see Table I). Their thicknesses were determined by weighting. The effective thickness in the region of the beam spot of about 4 mm diameter was controlled with the energy loss [9] of ^{241}Am α-particles; these values agreed within 5% with those of Table I (exception: ^{92}Mo, +15%; ^{94}Mo, +12%).

Table I: Target foils and isotopic composition

Target	thickness (mg/cm^2)	isotopic constituents (%)						
		92	94	95	96	97	98	100
^{92}Mo	3.79	98.52	0.36	0.35	0.29	0.16	0.37	0.14
^{94}Mo	2.64	0.87	94.60	2.50	0.98	0.32	0.55	0.18
^{95}Mo	4.18	0.14	0.32	97.43	1.38	0.25	0.38	0.09
^{96}Mo	4.31	0.13	0.16	0.52	97.67	0.79	0.62	0.11
^{97}Mo	4.65	0.22	0.24	0.59	1.34	94.25	3.07	0.30
^{98}Mo	4.16	0.10	0.07	0.16	0.23	0.33	98.78	0.33
^{100}Mo	4.15	0.12	0.16	0.27	0.38	0.28	0.84	97.95

The electronics of a single neutron TOF detector were conventional. The block diagram of the combined electronics of all 8 detectors is shown in Fig. 2. A linear bias was set individually for each detector at a pulse height corresponding to a proton energy $E_{thr} \approx 1.0$ MeV. The exact positions were determined [8] with the Compton edges of γ sources (^{22}Na, ^{88}Y, ^{137}Cs, ^{207}Bi). Similarly, an upper threshold was set for each detector at a maximum proton recoil energy $E_0 \approx 15$-16 MeV. The photo multiplier signals were stabilized [10] with respect to

COMPLETE ELECTRONIC CIRCUIT OF THE NEUTRON TOF FACILITY

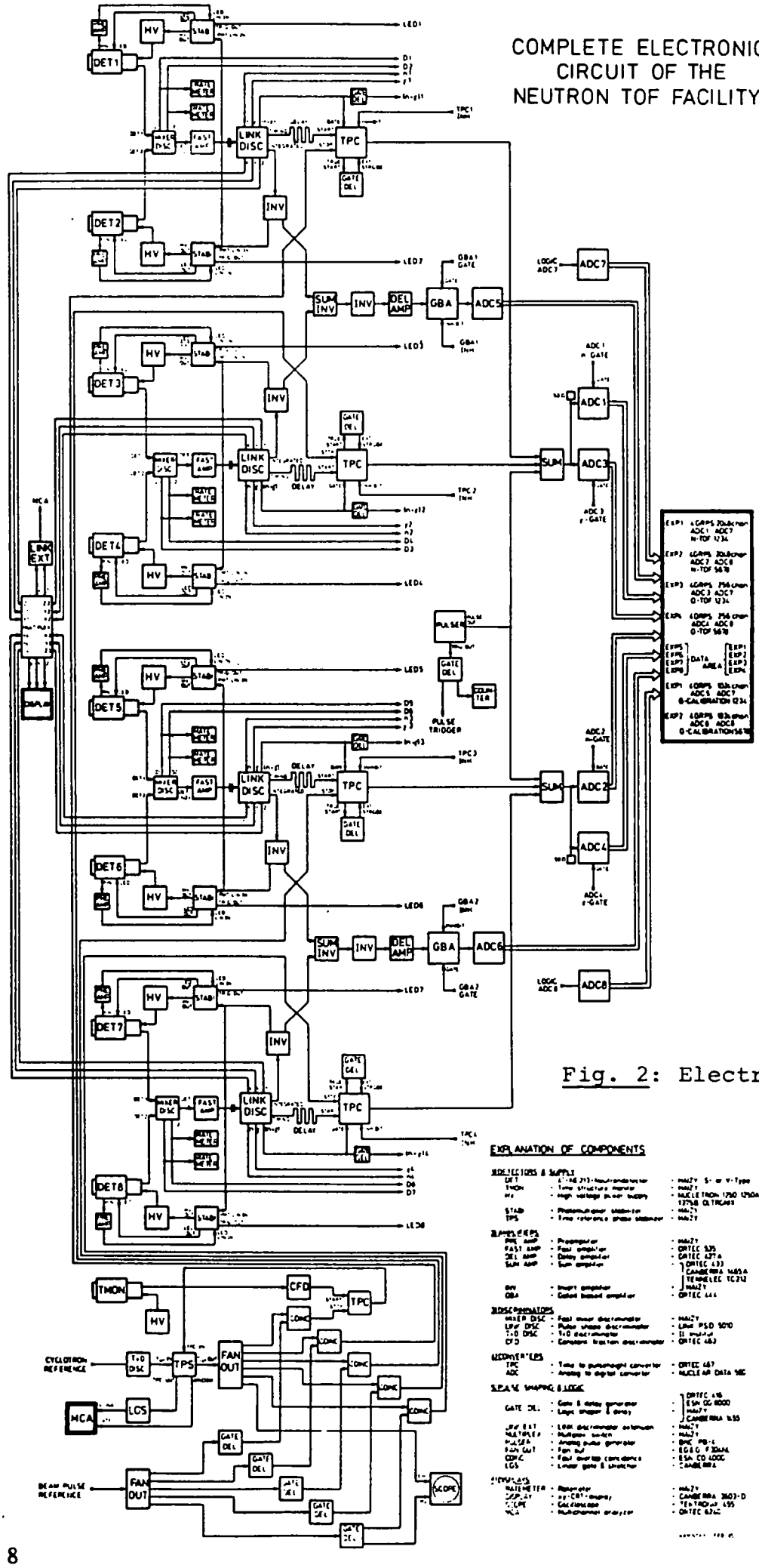

Fig. 2: Electronics diagram

EXPLANATION OF COMPONENTS

a stabilized LED. The γ radiation was effectively suppressed by pulse shape discrimination [11].

The TOF stop signal was derived from the cyclotron radio frequency. The TOF data for neutrons as well as for γ particles were routed via 8 ADC's into a ND4420 multichannel analyzer. The overall time resolution obtained was ≈ 1.5 ns (FWHM) corresponding to a neutron energy resolution of 60 keV (500 keV) for E_n = 5 MeV (20 MeV).

2.2. Measurements and data reduction

The measurements were performed with proton beam intensities of typically 30-50 nA. For each target and target position a total charge Q_{FC} of about 1 mC was accumulated in the Faraday Cup. Each run was followed by a shorter (Q_{FC} ≈ 0.5 mC) background run with shadow bars being placed in the flight paths about midway between target and detectors. The shadow bars are truncated polyethylene cones of 80 cm length (corresponding to 7 attenuation lengths λ for 15 MeV neutrons). However, for the extreme reaction angles 3^o and 177^o, respectively, carefully aligned shadow bars made out of copper (length: 50 cm, attenuation length for E_n = 15 MeV ≈ 10 λ), that were designed for mounting close to the target, were used instead to account for the worse background conditions due to the upstream beam line and the Faraday Cup, respectively.

Fig. 3 shows in the upper part some representative TOF spectra. The background subtraction represented at most a 10% correction of the integral yield in the physical region $E_{thr} \leq E_n \leq E_{n,max}$ and was substantial ($\leq$ 20%) only for the extreme angles and the high neutron energies. The energy scale is deduced from the position of the target γ peak and the time calibration of the

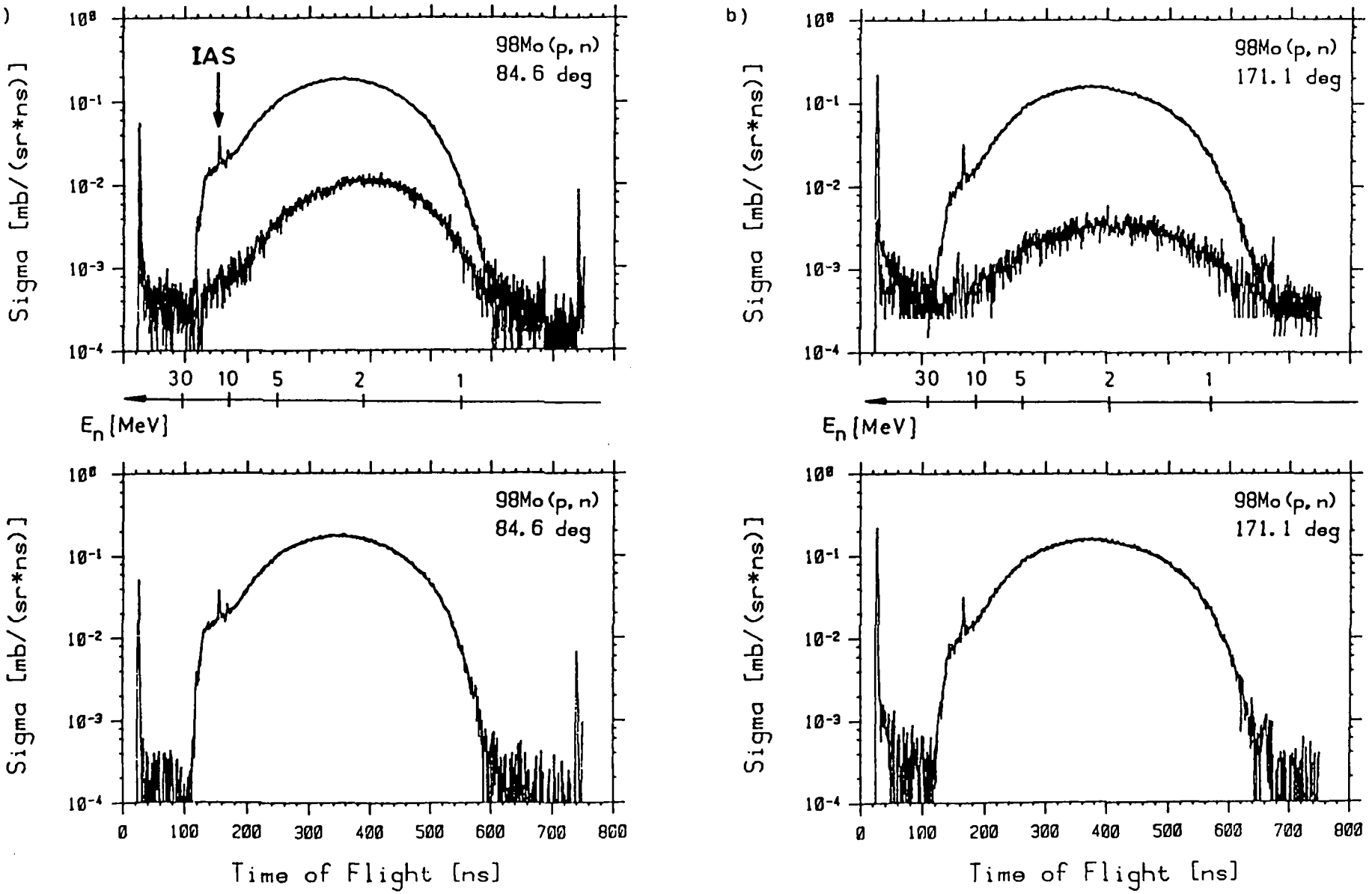

Fig. 3: Normalized neutron TOF spectra. Top: Run with target ^{98}Mo without and with shadow bar. Bottom: Effect spectrum (difference of the top line spectra).

system. In any case, the background spectra do not exhibit individual structures nor do they reflect the structures in the corresponding target in runs and therefore cannot be responsible for structures in the spectra, which remain after background subtraction. Further experimental details have been reported elsewhere [8,12].

Table II: Reaction data. Excitation energies E* (IAS) of the isobaric analogs are from Ref. 14 or, if in parentheses, calculated from Ref. 15. Maximum kinetic energies $E_{n,max}$ of the neutrons refer to the c.m.s.

Reaction	I^{π}_{Target}	$Q(p,n_0)$	$Q(p,n_1)$	$E^*(IAS)$	$E_{n,max}$
$^{92}_{42}Mo(p,n)^{92}_{43}Tc$	0^+	-8.65	-8.86	3.81	16.49
$^{94}Mo(p,n)^{94}Tc$	0^+	-5.04	-5.12	(7.3)	20.08
$^{95}Mo(p,n)^{95}Tc$	$5/2^+$	-2.48	-2.52	9.82	22.61
$^{96}Mo(p,n)^{96}Tc$	0^+	-3.76	-3.79	8.44	21.36
$^{97}Mo(p,n)^{97}Tc$	$5/2^+$	-1.10	-1.20	11.02	23.99
$^{98}Mo(p,n)^{98}Tc$	0^+	-2.46	-2.48	9.74	22.64
$^{100}Mo(p,n)^{100}Tc$	0^+	-0.95	-1.12	(10.9)	24.15

After background subtraction (cf. lower part of Fig. 3), the TOF spectra were converted with relativistic kinematics into center-of-mass energy spectra of bin size ΔE_n = 100 keV with the detector efficiencies calculated as described in [13] and under the assumption of single nucleon emission. The Q values and additional reaction data are listed in Table II. The shifts ΔE_n for neutrons actually resulting from second or third chance emission are at most equal to the recoil correction for the highest possible nucleon energy of $\approx$ 10 MeV (secondary emission), i.e. $|\pm\Delta E_n| \leq$ 150 keV. The rare events of neutrons following α particle emission are neglected.

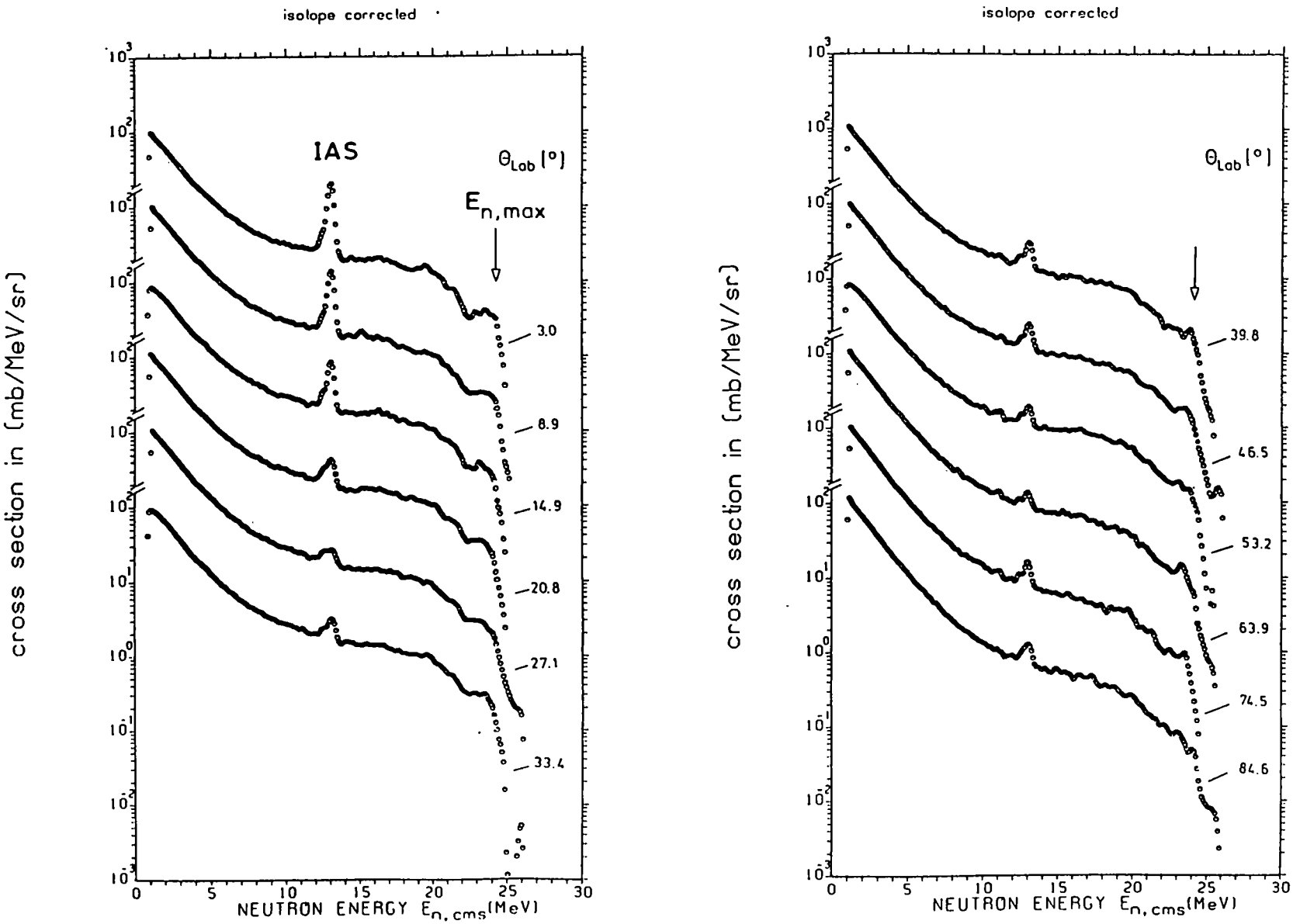

Fig. 4a: Double differential cross sections for ^{100}Mo(p,xn) and $0^{o} < \Theta_{lab} < 90^{o}$.

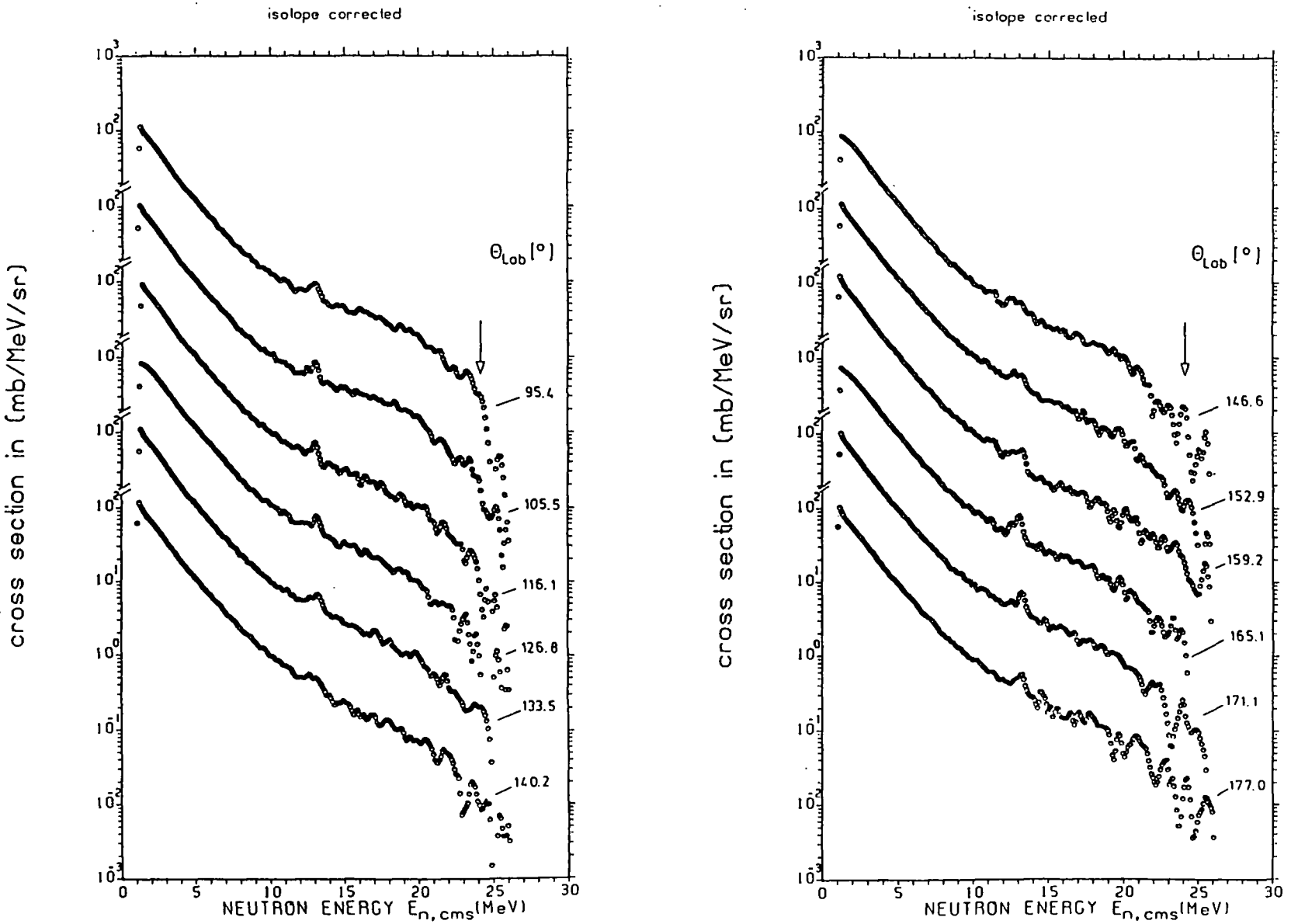

Fig. 4b: Double differential cross sections for ^{100}Mo(p,xn) and $90^{o} < \Theta_{lab} < 180^{o}$.

Having determined the sets of 24 energy spectra for all 7 molybdenum targets with known isotopic composition (Table I), one can calculate for each bin the double differential cross sections for isotopically pure material from a system of 7 linear equations. All cross sections presented furtheron are unfolded this way.

A representative set of spectra obtained at all 24 angles for p+^{100}Mo is shown in Fig. 4a,b. All spectra for ^{100}Mo as well as those for the 6 lighter isotopes show the isobaric analog ground state transitions (IAS), whose positions and widths confirm the correct and consistent transformation of the time into the neutron c.m. energy spectra and the energy resolution stated above.

Angle integrated neutron energy spectra were calculated as

$$\frac{d\sigma}{dE_n} = \sum_{\nu=1}^{24} \frac{d^2\sigma}{dE_n d\Omega}\cdot(\Theta_\nu, E_n)\cdot\omega(\Theta_\nu) \qquad (1)$$

with the solid angle weighting for $2 \leq \nu \leq 23$:

$$\omega(\Theta_\nu) = 2\pi\cdot\left[\cos\frac{\Theta_\nu+\Theta_{\nu-1}}{2} - \cos\frac{\Theta_{\nu+1}-\Theta_\nu}{2}\right] \qquad (2)$$

and for $\nu = 1$ or 24:

$$\omega(\Theta_\nu) = 2\pi\cdot\left(1 - \cos\frac{\Theta_\nu+\Theta_{\nu'}}{2}\right) \qquad (3)$$

where $\nu' = 23$ (or 2) for $\nu = 24$ (or 1).

The resulting set of angle integrated neutron energy spectra is shown in Fig. 5.

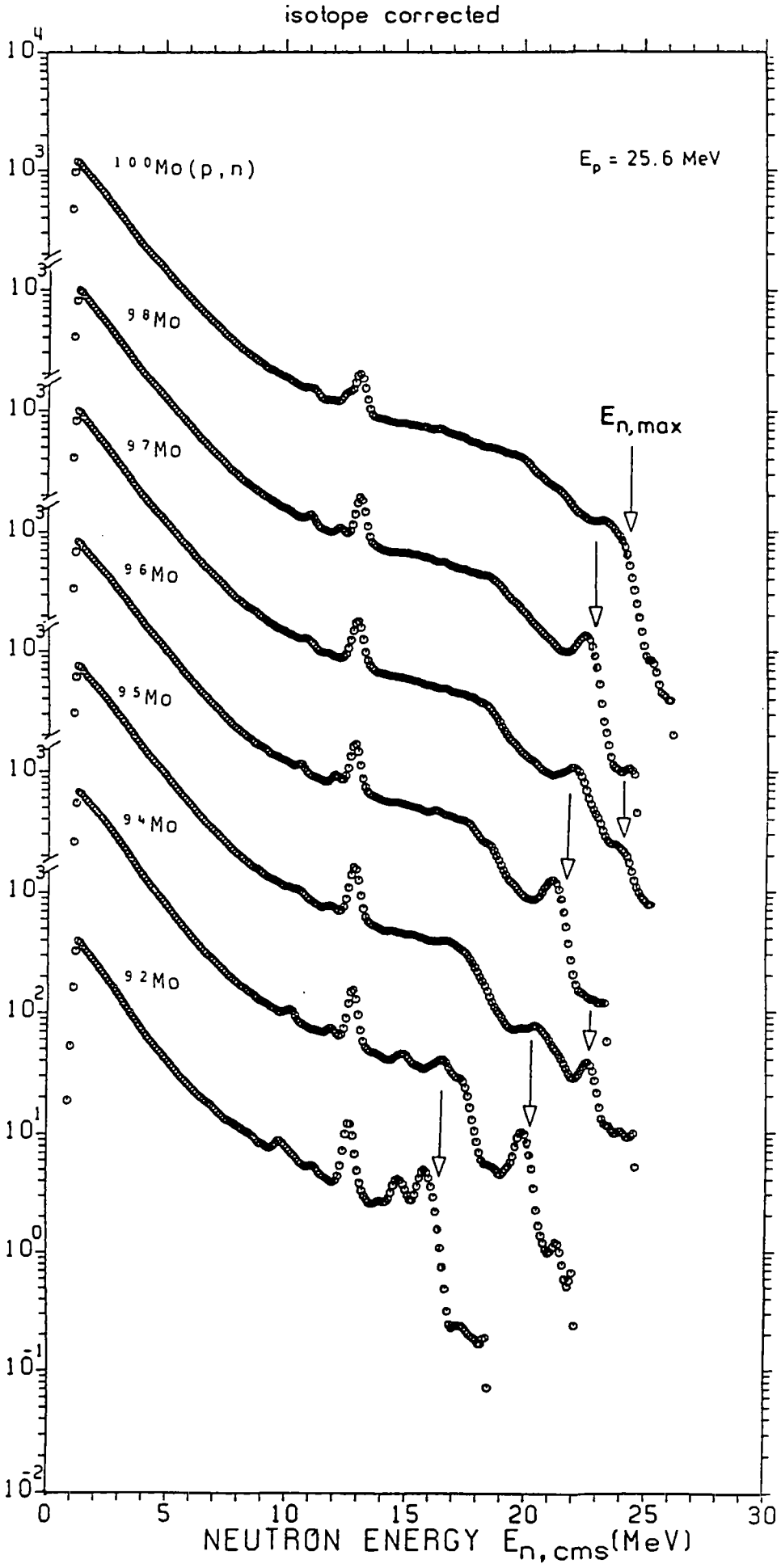

Fig. 5: Angle integrated neutron energy spectra for $^{92-100}$Mo(p,xn).

2.3. Uncertainty estimates and explanation of tables

The main uncertainty sources and their estimates are:

(1) Neutron detector efficiency 5%

(2) Effective target thickness (due to inhomogeneities and uncertainties of the range-energy tables) 5%

(3) Inconsistencies in the background treatment 5%

(4) Statistical uncertainties (< 1% for $E_n \leq 6$ MeV; < 4% for $E_n \leq 15$ MeV [exception: ^{92}Mo, 7% for $E_n \approx 15$ MeV and $\Theta = 177^{\circ}$]; <10% for $E_n \leq 20$ MeV) < 10%

(5) Incomplete beam current integration 3%

The estimated relative uncertainties between neutron spectra obtained in different runs are due to (2) - (5) and should not exceed 10% for all angles and all but the highest neutron energies. Absolute uncertainties are slightly higher due to contribution (1). Therefore we claim absolute uncertainties $\leq$ 12% for most of the double differential and all angle integrated cross sections.

References

[1] E. Mordhorst, M. Trabandt, A. Kaminsky, H. Krause, W. Scobel, R. Bonetti and F. Crespi, Phys. Rev. C34(1986)103

[2] T. Seo, H. Lawin, G. Lhersonnean, R.A. Meyer, G. Menzen and K. Sistemich, Z. Physik A320(1985)393

[3] W. Scobel, M. Blann, T.T. Komoto, M. Trabandt, S.M. Grimes, L.F. Hansen, C. Wong and B.A. Pohl, Phys. Rev. C30(1984)1480

[4] S.M. Grimes, J.D. Anderson,and C. Wong, Phys. Rev. C13(1976)2224

[5] M. Blann, W. Scobel and E. Plechaty,
Phys. Rev. C30(1984)1493

[6] R. Bonetti and L. Colli-Milazzo,
Proc. Workshop on Coincident Particle Emission from
Continuum States (COPECOS), Bad Honnef, 1984, p. 174

[7] H. Krause, R. Langkau and N. Schirm,
Nucl. Instr. Meth. 134(1976)15

[8] Y. Holler, A. Kaminsky, B. Scharlemann, H. Krause, R. Langkau,
W. Peters, G. Poppe, N. Schirm, W. Scobel and R. Wien,
Nucl. Instr. Meth. A235(1985)123

[9] J.F. Ziegler: Helium Stopping Powers and Ranges in All
Elemental Matter (Pergamon Press, 1977)

[10] Y. Holler, J. Koch and A. Naini,
Nucl. Instr. Meth. 204(1983)485

[11] J.M. Adams and G. White,
Nucl. Instr. Meth. 156(1978)459

[12] Y. Holler, A. Kaminsky, R. Langkau, W. Scobel, M. Trabandt
and R. Bonetti, Nucl. Phys. A442(1985)79

[13] G. Dietze and H. Klein,
Report PTB-ND-22 (Braunschweig, 1982)

[14] W.J. Courtney and J.D. Fox,
At. Data Nucl. Data Tables 15(1975)141

[15] J.D. Anderson, C. Wong and J.W. McClure
Phys. Rev. 138(1965)B615